Optimized magneto-optical isolator designs inspired by seedlayer-free terbium iron garnets with opposite chirality

Prabesh Dulal,[*,†] Andrew D. Block ,[‡] Thomas E. Gage ,[†] Harold A. Haldren ,[§] Sang Yeob Sung ,[‡] David C. Hutchings,[‖] Bethanie. J. H. Stadler [*,†,‡]

[†]Chemical Engineering and Materials Science, University of Minnesota, Minneapolis, MN, U.S.A.

[‡]Electrical and Computer Engineering, University of Minnesota, Minneapolis, MN, U.S.A.

[§] School of Engineering, Liberty University, Lynchburg, Virginia, U.S.A.

[‖]School of Engineering, University of Glasgow, Glasgow, Scotland, U.K.

ABSTRACT: Simulations demonstrate that undoped yttrium iron garnet (YIG) seedlayers cause reduced Faraday rotation in silicon-on-insulator (SOI) waveguides with Ce-doped YIG claddings. Undoped seedlayers are required for the crystallization of the magneto-optical Ce:YIG claddings, but they diminish the interaction of the Ce:YIG with the guided modes. Therefore new magneto-optical garnets, terbium iron garnet (TIG) and bismuth-doped TIG (Bi:TIG), are introduced that can be integrated directly on Si and quartz substrates without seedlayers. The Faraday rotations of TIG and Bi:TIG films at 1550nm were measured to be +500 and -500°/cm, respectively. Simulations show that these new garnets have the potential to significantly mitigate the negative impact of the seedlayers under Ce:YIG claddings. The successful growth of TIG and Bi:TIG on low-index fused quartz inspired novel garnet-core waveguide isolator designs, simulated using finite difference time domain (FDTD) methods. These designs use alternating segments of positive and negative Faraday rotation for push-pull quasi phase matching in order to overcome birefringence in waveguides with rectangular cross-sections.

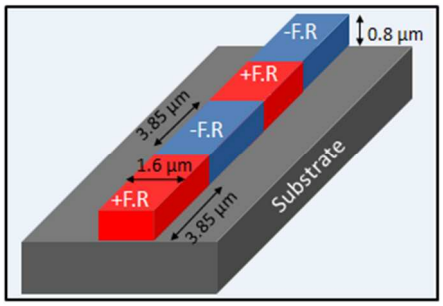

KEYWORDS: yttrium iron garnet (YIG) seedlayer, terbium iron garnet (TIG), cerium doped yttrium iron garnet (Ce:YIG) , silicon on insulator (SOI) waveguides, Faraday rotation, optical isolator

Photonic systems have ever increasing applications in high-speed electronics/ spintronics [1,2], computing [3], telecommunications [4,5] and medicine [6]. These systems use light as the signal carrier, and similar to diodes in electronics, photonic systems require non-reciprocal devices with high optical isolation capabilities to protect light sources. Currently, non-reciprocal photonic materials are only available in discrete components. However, if light sources are to be integrated onto photonic chips, non-reciprocal devices will also be needed on those chips. Indeed, isolators will be necessary anywhere in optical circuits where back-reflections are detrimental and likely to occur.

Garnets, with their unique magneto-optical (MO) properties have been the material of choice for building passive non-reciprocal devices [7–10]. In general, non-garnet non-reciprocal devices are active devices that require external power sources, which increase the complexity and cost of the device [11–14]. MO effects in garnets are the result of non-zero off-diagonal components in the dielectric matrix (ε) which break time-reversal symmetry. The diagonal components ($\varepsilon_{xx}=\varepsilon_{yy}=\varepsilon_{zz}$) are essentially the squares of the indices of refraction ($n_{xx}=n_{yy}=n_{zz}=n$ for isotropic materials), and off-diagonal components (eg: ε_{xz}) can be measured by Faraday rotation (θ_F): $\varepsilon_{xz}=(n\lambda\theta_F)/\pi$, where λ is the wavelength. Although other materials can have higher ε_{xz} [15,16], they also have much higher losses, so the optimal device performances have been achieved with garnets.

Garnet photonic isolators can be placed into two categories: semiconductor-core devices, where a garnet cladding provides the nonreciprocity, and garnet-core devices. In either category, one of two magneto-optical effects are typically employed: nonreciprocal phase shift (NRPS) or Faraday rotation. NRPS occurs in a transverse magnetic field [17], and it can be utilized for optical isolation using interferometer [18] or ring resonator [19] designs. Faraday rotation is a nonreciprocal rotation, or mode conversion, that occurs with a magnetic field parallel to the propagating light, and it can provide isolation together with a simple polarizer at the input of a waveguide [20,21].

Almost all of the recent devices in both categories have employed Ce:YIG as the MO material [8,19,21–26]. In the first category, isolators based on Mach-Zehnder interferometers have been developed by bonding Ce:YIG onto Si-on-insulator (SOI) waveguides by surface-activated [18] or adhesive [22] bonding. Ce:YIG claddings have also been used in the development of SOI ring resonators [19,25–28], Si_3N_4-core circulators [29], and SOI- or III-V-core Faraday rotators [21]. Garnet-core waveguide devices have included NRPS interferometers [24] and Faraday rotators [20,21].

From a commercial point of view, monolithically-integrated optical isolators are highly desirable because of their cost efficiency and processing convenience. The first monolithic Si-integrated isolator was achieved using was achieved using an SOI racetrack resonator with a Ce:YIG cladding [28]. However, monolithic integration of this doped garnet required a two-step deposition process in which an ultra-thin (≈ 20 nm) seedlayer of undoped YIG was grown and annealed prior to deposition of the doped layer [30]. Attempting the growth of Ce:YIG without a seedlayer results in the formation of oxide phases other than garnet without useful MO properties[8]. Recently a one-step YIG/Ce:YIG anneal has also been reported [25] and will be discussed below.

In a semiconductor-core device, the waveguide has a higher index of refraction (n≈3) than the garnet layer (n≈2). As light propagates through the waveguide, the evanescent tail extends through the seedlayer before reaching Ce:YIG layer where the nonreciprocal interaction takes place. Such a seedlayer therefore limits the amount of light that reaches the Ce:YIG. Unfortunately, even with the seedlayer, most researchers report lower MO values (eg: -1263°/cm) [28] for this integrated Ce:YIG than that of a Ce:YIG grown on doped GGG (gadolinium gallium garnet) substrate by sputter epitaxy (-4500°/cm) [18,31]. The usual explanation is incomplete crystallization. Although wafer-bonded Ce:YIG (which is grown on garnet substrates) has full MO properties, the bonding method involves an adhesion layer that also reduces the interaction of the guided mode with the cladding.

Nonreciprocal photonic devices need to balance minimizing size while maximizing isolation ratio (IR). Some examples that highlight the race for improved device design are: a 4mm long Si interferometer with wafer-bonded Ce:YIG (IR=17dB) [18], a 1.8mm (diameter) silicon ring with wafer-bonded Ce:YIG (IR=9dB) [19] and a 920μm long Si interferometer with adhesive-bonded Ce:YIG (IR=25dB) [22]. The shortest reported isolator device to date is a 290μm Si ring resonator with a sputtered Ce:YIG cladding (IR= 19.5dB) [28]. However, these NRPS devices only operate with one mode, typically transverse magnetic (TM) unless side-coating can be achieved [32]. Theoretically, the shortest Ce:YIG Faraday rotator would involve a garnet-core with the full -4500 °/cm, and therefore it would be 100μm long to achieve the 45° rotation required for isolation. However, if light propagating inside a Faraday rotating waveguide experiences birefringence, full mode conversion may not be possible. Such birefringence has been overcomed in 8mm long III-V waveguide devices using quasi-phase matching, where the cladding had garnet-silica segmentation along the guide (IR=0.9-1.2dB/mm) [33]. Improved crystallization of the garnet later yielded full mode conversion in 3mm [21]. Importantly, once highly gyrotropic YIG is grown successfully on Si, it may also find application in spintronics, for example, in spin logic and spin current generators[1,34–44].

This paper will discuss the optical consequences of having seedlayers on waveguides with garnet claddings and will introduce two new garnet materials, terbium iron garnet (TIG, $Tb_3Fe_5O_{12}$) and bismuth-doped terbium iron garnet (Bi:TIG), both of which do not require seedlayers on Si or on other non-garnet substrates. The successful growth and characterization of these garnets will be discussed, and their resulting MO properties will be used in simulations to show their potential impact on photonic isolators. First, different seedlayers for Ce:YIG claddings on SOI waveguides will be simulated by the modesolver technique presented in Ref. 45. Next, garnet-core designs with push-pull quasi phase matching will be simulated by Finite Difference Time Domain (FDTD). The results show that negative MO materials or materials with negative chirality of Faraday rotation, such as Bi:TIG, can significantly mitigate seedlayer effects in Ce:YIG-cladded waveguides and that large positive MO materials, such as TIG, can reduce the lengths of isolators using push-pull quasi-phase matching.

Simulations of seedlayer effect: Light propagation (TE-like mode) was simulated in SOI waveguides with 100nm claddings of Ce:YIG grown on YIG seedlayers (0-100nm) with a saturating magnetic field parallel to the light propagation. A cross section schematic of the device is shown in Figure 1 (a). Reported Faraday rotation coefficients were used, including 200°/cm [46] for the YIG seedlayer and a range of values (-1100°/cm [25], -1263°/cm [28], -3300 °/cm [47], -3700°/cm [48], -4500°/cm [31]) for the Ce:YIG layer. The lower values in this range are attributed to incomplete crystallization of Ce:YIG [28,32]. The average S_3 Stokes parameter [21,45], which provides the degree of nonreciprocal polarization mode conversion (and is directly related to ε_{xz}) for the TE-like polarized mode is calculated by finite-difference modesolver and shown in Figure 1(b) plotted against varying thicknesses of the YIG seedlayer. This allows for a direct comparison to be drawn between various configurations of MO (Ce:YIG) and seed (YIG) layers.

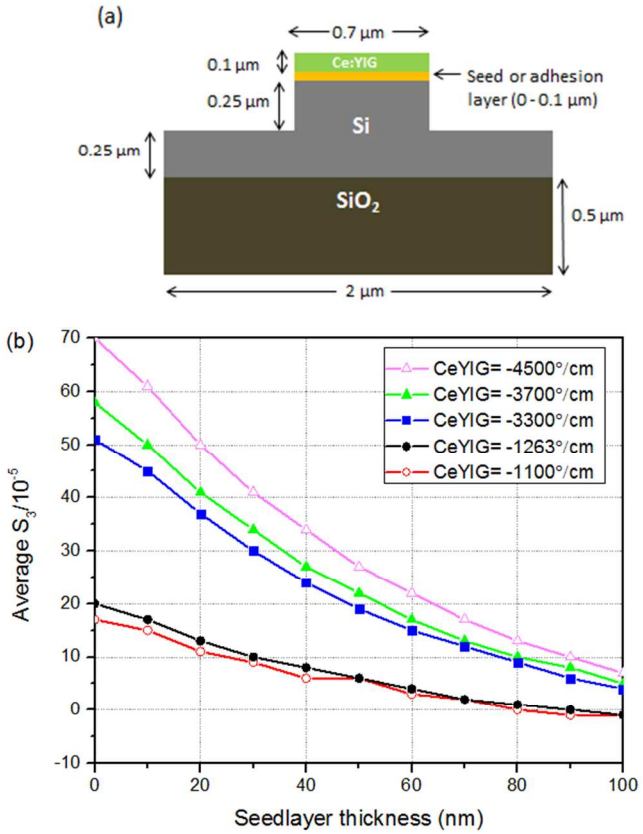

Figure 1. (a) Cross sectional schematic of SOI waveguide with garnet cladding. (b) Average S_3 Stokes parameters for TE-like modes in SOI waveguides with Ce:YIG/YIG claddings plotted vs. thickness of YIG seedlayer. The claddings use 0-100nm YIG seedlayer (200 °/cm) and a fixed thickness (100 nm) Ce:YIG layer (varying Faraday rotation).

It has been shown that a YIG seedlayer must be at least 45nm thick for complete crystallization of a doped cladding [48]. However, the results shown in Figure 1 (b) suggest that even a 20nm-thin seedlayer, as used in Ref. 28, reduces the net MO effect of the garnet-cladded SOI waveguides by almost 30% (as seen in all of the curves by comparing 0 vs. 20nm seedlayer thickness). If a 45nm YIG seedlayer would allow complete crystallization of an ideal Ce:YIG cladding, thereby obtaining Faraday rotation as high as -4500 °/cm, 45nm would still separate the guided mode from the active cladding. Therefore, the S_3 parameter would be reduced by 57% (S_3 = 70 vs. 30 x10^{-5}) as shown by the pink curve ($t_{seedlayer}$ = 0 vs. 45nm) in Figure 1(b). The net MO effect is comparable to a cladding with only -2000 °/cm and no seedlayer, which has not been achieved to date. In fact, these simulations show that the best Ce:YIG cladding material to date is the -3700°/cm Ce:YIG that required a 45nm YIG seedlayer [48]. Figure 1(b) shows that this cladding will lead to almost twice the S_3 parameter, which means twice the effective MO mode conversion per unit length than the next lowest reported value for bottom-seeded Ce:YIG (on Si), -1263°/cm [28] (S_3 = 25 vs. 13 x10^{-5}). This can be seen from the green ($t_{seedlayer}$ = 45nm) and black ($t_{seedlayer}$ = 20nm) curves.

In addition to reducing the MO effect, the seedlayer also adds processing steps. In most reports, the seedlayer is annealed outside of the processing vacuum before the Ce:YIG cladding can be deposited. As mentioned in the introduction, however, a one-step YIG/Ce:YIG anneal was recently introduced that works even when the undoped YIG seed is on top of the cladding (and therefore not between the cladding and the guide). Unfortunately, the Faraday rotation of that Ce:YIG was only -1100°/cm [25], so it is 36% less effective than the -3700°/cm Ce:YIG (45nm seedlayer) that was determined to be the best cladding above (S_3 = 25 vs. 16 x10^{-5}). This can be seen in Figure 1(b) from the green ($t_{seedlayer}$ = 45nm) and red ($t_{seedlayer}$ = 0nm) curves.

A final concern with YIG seedlayers is that they have Faraday rotation of opposite chirality to that of Ce:YIG. The dramatic results in Figure 1 (b) indicate that the YIG layers are not simply optical dead space; they are actually detrimental to the Ce:YIG performance. These factors stress the importance of finding magneto-optical garnets on semiconductor waveguides that either (1) do not require seedlayers, or (2) have seedlayers with the same chirality as Ce:YIG claddings.

Fabrication and characterization of terbium iron garnets: TIG and Bi:TIG thin films were fabricated on Si and quartz substrates using radio frequency (RF) reactive sputter deposition with an Ar/O_2 plasma followed by rapid thermal anneal (RTA). For the fabrication of TIG, an Fe target was sputtered at 220W and a Tb target was sputtered at 120W. For Bi:TIG, the Fe target was sputtered at 220W and the Tb and Bi targets were sputtered at 110W and 10W, respectively. The deposition was performed with 20.4 sccm Ar and 2.0 sccm O_2 flow, and the chamber pressure was held at a constant 2.0 mTorr. Films were post annealed (RTA) for two minutes at 900°C in an O_2 atmosphere.

The crystallographic structure of resulting films was characterized using X-Ray diffraction, which confirmed the formation of single phase garnet on Si and quartz substrates (Figure 2). The stoichiometry of the TIG film was measured to be $Tb_{0.35}Fe_{0.65}O_{12}$ and that of the Bi:TIG film was measured to be $Bi_{0.05}Tb_{0.31}Fe_{0.64}O_{12}$ using energy dispersive x-ray spectroscopy (EDS). A detailed analysis of composition vs. crystallinity of other phases observed en route to the development of the TIG and Bi:TIG phases are given in the supplementary information (Figure S1 (TIG) and Figure S2 (Bi:TIG)). Next, Ce:YIG was successfully grown on Bi:TIG seedlayer (supplementary information, Figure S3).

In-plane and normal-to-plane magnetic hysteresis of thin films demonstrating their ferromagnetic nature were measured using a Vibrating Sample Magnetometer (VSM), sweeping the magnetic field from +5000 Oe to -5000 Oe (Figure 3). Faraday rotation measurements were carried out at 1550nm using magnetic fields from +2000 to -2000 Oe. The Faraday rotation of TIG was measured to be 500°/cm, whereas that of Bi:TIG was -500°/cm.

Terbium iron garnets: seedless claddings or ideal seedlayers for Ce:YIG claddings? Modesolver simulations were performed to compare the impact of various seedlayers on the net MO effect observed in SOI waveguides with Ce:YIG top claddings whose cross-sectional schematic is shown in Figure 1(a). Figure 4 shows how the average Stokes (S_3) parameter varies with seedlayer thickness for Ce:YIG claddings with different reported values of Faraday rotation: -1263°/cm [28], -3700°/cm [48] and -1100°/cm [25].

For the first two cases (-1263°/cm and -3700°/cm Ce:YIG), the seedlayers (bottom) are between the guide and the Ce:YIG cladding whose thickness was kept constant at 100nm and the seedlayers were varied from 0-100 nm. For the third case

(-1100°/cm Ce:YIG, green), the YIG seedlayer is not between the guide and the cladding but is rather on top of the Ce:YIG . Here the Ce:YIG thickness was varied from 100-200nm. For the fourth case, (-500 °/cm Bi:TIG, pink) there was no seedlayer involved, but the Bi:TIG itself was varied from from 100-200nm.

Figure 4 demonstrates that seedlayers with opposite chirality have detrimental impact on the net MO effect as seen by comparing seedlayers with +200 °/cm (YIG, black curves), 0°/cm (eg: adhesion layers, red curves) and -500 °/cm (Bi:TIG, blue curves).

Table 1 gives a summary of some of the Ce:YIG/YIG claddings simulated in Figure 4. The discovery of (iii) is extremely impressive. It uses a single anneal and does not involve a layer between the waveguide and cladding. As seen from the green curve in Figure 4, if grown thick enough (>180nm), this cladding could have comparable MO effect as (ii). Here, the evanescent tail interacts directly with the Ce:YIG layer without having to pass through the bottom YIG seedlayer, and hence the S_3 parameter gets better with increasing thickness of Ce:YIG. The mode is confined within the Ce:YIG and doesn't reach the top YIG, and thus the opposite chirality of YIG doesn't affect the mode conversion. However, the question is whether the Ce:YIG cladding can have high quality crystallinity at the interface with the guide when the seeding occurs from the top of this thick cladding. Even so, (iii) has more than twice the S_3 parameter and hence more than twice the MO impact on mode conversion than (vi). Therefore, Bi:TIG will not be an effective seedless cladding unless minimal processing steps (i.e.: a single layer cladding with one anneal) are more desirable than a short device length. However, a Bi:TIG seedlayer improves modal interaction for (v) by 38% (S_3= 18 vs. 13/10^{-5}) and for (ii) by 32% (S_3= 33 vs. 25/10^{-5}). Therefore, (ii) has the maximum non-reciprocal effect among all of these reported Ce:YIG MO claddings, especially if Bi:TIG is used as a seedlayer. This shows that seedlayer chirality is an important factor that has been overlooked in the literature to date.

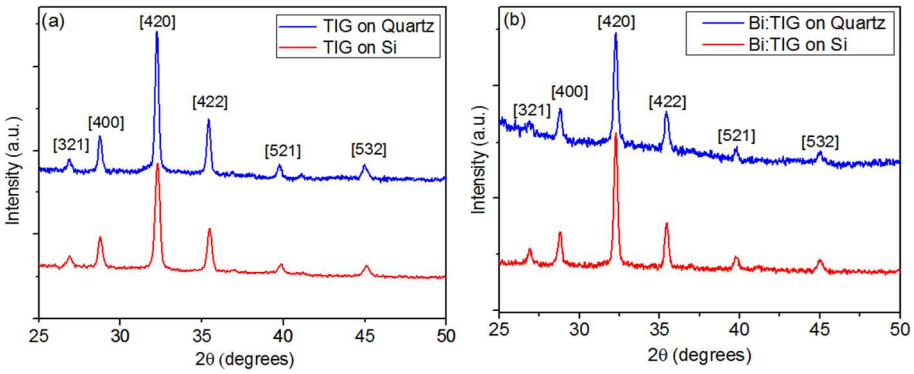

Figure 2. X-Ray diffraction patterns of (a) TIG and (b) Bi:TIG films on Si and quartz substrates confirming the single phase garnet.

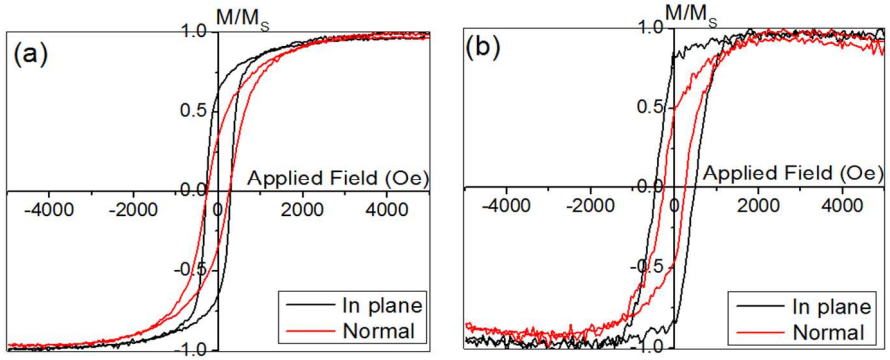

Figure 3. Magnetic hysteresis loops of (a) TIG and (b) Bi:TIG films measured using a VSM demonstrating the ferromagnetic property of the films.

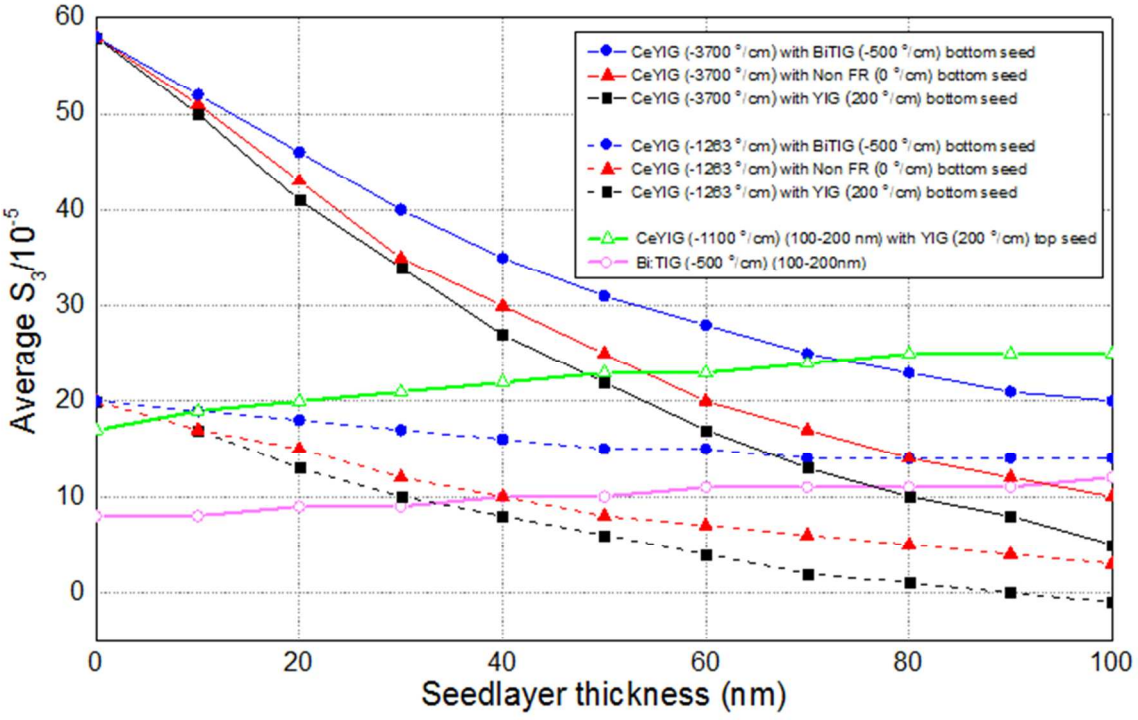

Figure 4. Seedlayer thickness plotted against average S_3 Stokes parameters for TE-like modes in SOI waveguides (schematic in Figure 1a) with different combinations of garnet claddings. Devices with different reported values of Ce:YIG (-1100°/cm [25], -1263°/cm [28] and -3700°/cm [48]) grown on YIG (+) seedlayers are simulated and compared with devices that use non FR (0) seedlayers and Bi:TIG (-)seedlayers.

S.N.	Seed material	Seed thickness (nm)	Ce:YIG cladding θ_F (°/cm)	S_3 ($/10^{-5}$)	Corresponding curve in Figure 4	Reference.
i	Bi:TIG	45	-3700	33	blue, solid	Simulation
ii	YIG	45	-3700	25	black, solid	48
iii	YIG	top seed (30)	-1100	25	green	25
iv	Bi:TIG	20	-1263	18	blue, dotted	Simulation
v	YIG	20	-1263	13	black, dotted	28
vi	Bi:TIG	no seed	-500	<12	pink	This work

Table 1. Summary of the specific YIG seedlayer thicknesses used in literature along with their corresponding simulated average S_3 Stokes parameters. Table demonstrates how the S_3 parameter significantly improves for the Ce:YIG grown on Bi:TIG seedlayer.

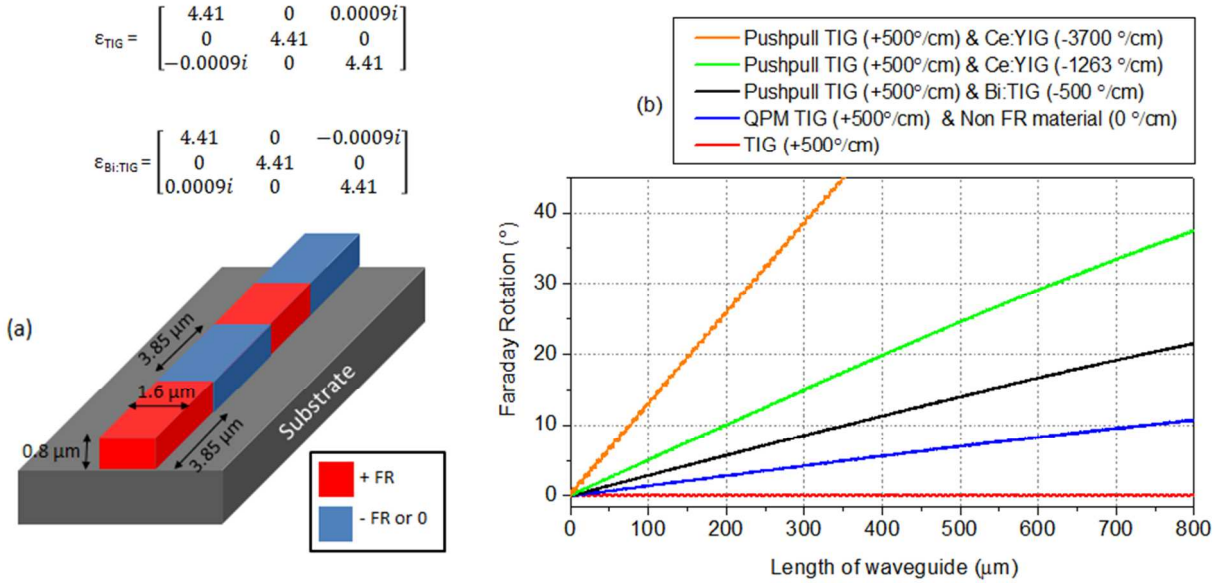

Figure 5 (a) Schematic of quasi-phase matched (QPM: +FR & 0) and push-pull (+FR & -FR) garnet waveguides. Here, +FR and -FR refer to segmented materials with positive and negative chirality of Faraday rotation and 0 refers to materials that don't exhibit any Faraday rotation (b) FDTD simulations of TIG, QPM TIG and different combinations of push-pull garnet waveguides of 1.6 µm x 0.8 µm cross section. The QPM and push-pull waveguides have 3.85 µm long strips on fused quartz substrate.

FDTD designs and simulations of garnet-core waveguides: The discovery of these novel TIG films with equal, but opposite Faraday rotation chirality inspired a new design for quasi phase matching (QPM) [21,33]. QPM is a technique that can be used to eliminate the birefringence effects caused when waveguide cross sections are anisotropic. For example, slow growth rates make it difficult to deposit thick films, and photolithography can limit the ability to decrease waveguide widths, making square cross sections difficult to fabricate. Furthermore, isotropic waveguide cross-sections may be undesirable in semiconductor-core waveguides as polarization-mode scattering is enhanced, which can compromise the coherence of the Faraday rotation. The anisotropic shape leads to differences in the propagation constants of TE and TM modes, and a limited, periodic mode conversion occurs as the light propagates (eg: red curve in Figure 5b). QPM is a design in which the waveguide is segmented (Figure 5a), with Faraday rotating (FR) and non-FR materials along the length of the waveguide with half the periodicity of the modal conversion (also called the beat-length) [21,33]. The novel design presented here will use segments with opposite Faraday rotation chirality, which can be considered as equivalent to the role of domain reversal in nonlinear optical frequency conversion.

Waveguide devices were designed using Finite Difference Time Domain (FDTD) simulations. Using the measured optical proper properties of TIG and Bi:TIG, the dielectric permittivity tensors, ε_{TIG} and $\varepsilon_{Bi:TIG}$ for these simulations were constructed with n = 2.1, λ = 1550nm , Faraday rotation (TIG) = 500°/cm and (Bi:TIG) = -500°/ cm. Fused quartz (n = 1.46) was used as the substrate material.

Simulations were performed using garnet waveguides with 2:1 aspect ratios (1.6 µm wide x 0.8 µm thick). These dimensions are easy to fabricate, and present an extreme shape anisotropy compared to an isotropic (square) cross section. When the whole length of the waveguide is TIG, propagating light only rotates a fraction of a degree before returning to zero in a periodic fashion with a beat length of 7.7µm, shown by the red line in Figure 5(b). When propagating down a QPM waveguide, light encounters a new material at each point when it would otherwise rotate back to zero, namely every half beat-length (3.85µm). QPM TIG was simulated

with +500 and 0 °/cm segments (blue line in Figure 5b). This shows the ability of standard QPM to overcome birefringence, although not fully recovering the isotropic Faraday rotation. The opposite chiralities of TIG and Bi:TIG enables QPM to be extended into a novel "push-pull" garnet waveguide that provides much higher net Faraday rotation, as shown by the black line in Figure 5(b).

Push/pull QPM isolators were also simulated using TIG and monolithically-integrated Ce:YIG, which has much higher reported values of Faraday rotation (-1263°/cm [28] and -3700°/cm [48]). These devices had the same (1.6 μm x 0.8 μm) cross-sections. TIG and Ce:YIG segments were alternated every 3.85μm. The results, shown in Figure 5(b) indicate that these devices give rise to a full 45° Faraday rotation using a much smaller device lengths using bottom-seeded Ce:YIG, including only 350 μm using the -3700°/cm [48] Ce:YIG (orange). Full modal conversion (equal to 90° Faraday rotation) would then be reached by backward propagating light (45° forward + 45° backward) such that the reflection would be blocked by any polarization selecting device.

Fabrication tolerance: As with interferometer designs, fabrication tolerances could be an issue for device performance. However, here the issue is not length variations as with interferometers, but cross sectional variations. The periodicity of the QPM waveguide is determined by the differences that arise in the propagation constants of TE and TM modes due to the asymmetry of the height and width. This problem was addressed in the early days of YIG waveguide devices (on GGG) when birefringence was overcome by etch tuning methods[49,50]. Here, one could pattern QPM strips, and then pattern the guides. If the fabricated width/height ratio doesn't quite match the QPM beatlength, the thickness of the guide would simply be etch-tuned until performance matches specifications.

It is often most economical to use thin films (small height) due to slow deposition rates and wide waveguides (large widths) due to inexpensive photolithography limits. In Figure 5, QPM results are shown for very practical dimensions (H=0.8 um and W=1.6um). These dimensions determine the device birefringence (that is, differences in TE vs TM propagation constants), which in turn determines the QPM beatlength. To estimate the fabrication tolerances on the proposed devices, various widths and heights were simulated. The results are presented in Supplemental Information Figures S4, S5 and S6. In short, a waveguide that is within +/- 10nm in width (Figure S4) of the intended value could be etched back to a height that is within +/- 2nm of the matching QPM height (Figure S5) to regain full performance. Control of garnet etch rates is straightforward using temperature during a phosphoric acid etch (1nm/sec at 120°C[49] and slower at room temperature), so this tolerance would be easy to obtain. To verify this technique, a matching width/height pair was simulated (Figure S6) to show full device performance. Once optimized, it is important to appreciate that, unlike interferometers, these devices allow complete polarization diversity, meaning they can be applied for all polarizations from TE to TM photonic integrated circuits.

Conclusions: Ce- and Bi-doped YIG films have dominated the field of magneto-optical materials for photonic non-reciprocal devices. However, these films require undoped YIG seedlayers when integrated with non-garnet substrates. Our simulations show that these seedlayers can significantly counteract the non-reciprocity brought about by the doped garnets in SOI devices. Simulations were also used to compare modal interactions with various published MO cladding/seedlayer pairs, and the best monolithic cladding to date uses 45nm YIG seedlayers to produce Ce:YIG with -3700°/cm of Faraday rotation [48]. To mitigate seedlayer issues, two new seedlayer-free garnets, TIG and Bi:TIG, were presented here. These garnets can be used as single-layer claddings for ease of manufacturing with either positive or negative nonreprocity and Bi:TIG was shown to be an excellent seedlayer for Ce:YIG with matching chirality. Furthermore, TIG and Bi:TIG were successfully grown on lower refractive index fused quartz substrates, so they can be easily used in garnet-core devices with push-pull quasi phase matching to eliminate birferengince effects. This novel idea of using two different materials with opposite MO chirality has opened doors for the reduction in device footprint while also allowing for the polarization-diverse (TE-TM) isolators.

ASSOCIATED CONTENT

Supporting Information

(1)Compositional study of the different phases obtained en route to the development of TIG & Bi:TIG films (EDS and XRD results). Given in Figures S1 and S2

(2) XRD and EDS results of Ce:YIG films grown on Bi:TIG seedlayer. Given in Figure S3.

(3) FDTD simulations demonstrating fabrication tolerance on TIG (+500°/cm) and Ce:YIG(-3700°/cm) QPM waveguide. Given in Figures S4 , S5 and S6.

The supporting information is available free of charge via the internet at http://pubs.acs.org.

AUTHOR INFORMATION

Corresponding Authors

*Email: dulal002@umn.edu

*Email: stadler@umn.edu

Author Contributions

The manuscript was written through contributions of all authors. All authors have given approval to the final version of the manuscript.

Notes

The authors declare no competing financial interests.

ACKNOWLEDGEMENTS

This work was supported primarily by the National Science Foundation through the University of Minnesota MRSEC under Award Number DMR-1420013, and was supported partially by National Science Foundation via the World Materials Network: DMR-1210818. Parts of this work were carried out in the UMN Characterization Facility. The authors would like to thank the Minnesota Nanofabrication Center (MNC) staff for their valuable support and are grateful for resources from the Minnesota Supercomputing Institute (MSI).

REFERENCES

(1) Kajiwara, Y.; Harii, K.; Takahashi, S.; Ohe, J.; Uchida, K.; Mizuguchi, M.; Umezawa, H.; Kawai, H.; Ando, K.; Takanashi, K.; Maekawa, S.; Saitoh, E. Transmission of Electrical Signals by Spin-Wave Interconversion in a

Magnetic Insulator. *Nature* **2010**, *464*, 262–266.

(2) Almeida, V. R.; Barrios, C. A.; Panepucci, R. R.; Lipson, M. All-Optical Control of Light on a Silicon Chip. *Nature* **2004**, *431*, 1081–1084.

(3) Rong, H.; Liu, A.; Jones, R.; Cohen, O.; Hak, D.; Nicolaescu, R.; Fang, A.; Paniccia, M. An All-Silicon Raman Laser. *Nature* **2005**, *433*, 292–294.

(4) Liu, X.; Osgood, R. M.; Vlasov, Y. a.; Green, W. M. J. Mid-Infrared Optical Parametric Amplifier Using Silicon Nanophotonic Waveguides. *Nat. Photonics* **2010**, *4*, 557–560.

(5) Pritchard, J. W.; Mina, M.; Dulal, P. Demonstration of Magnetooptic Latching Router for All-Optical Networking Applications. *IEEE Trans. Magn.* **2014**, *50*, 1–4.

(6) Yan, R.; Gargas, D.; Yang, P. Nanowire Photonics. *Nat. Photonics* **2009**, *3*, 569–576.

(7) Dillon, J. F. Origin and Uses of the Faraday Rotation in Magnetic Crystals. *J. Appl. Phys.* **1968**, *39*, 922–929.

(8) Stadler, B. J. H.; Mizumoto, T. Integrated Magneto-Optical Materials and Isolators: A Review. *IEEE Photonics J.* **2014**, *6*, 1–15.

(9) Fratello, V. J.; Wolfe, R. Epitaxial Garnet Films for Nonreciprocal Magneto-Optic Devices. In *Handbook of Thin Films, 4*; 2000; pp 93–141.

(10) Dotsch, H.; Bahlmann, N.; Zhuromskyy, O.; Hammer, M.; Wilkens, L.; Gerhardt, R.; Hertel, P.; Popkov, A. F. Applications of Magneto-Optical Waveguides in Integrated Optics: Review. *J. Opt. Soc. Am. B* **2005**, *22*, 240.

(11) Van Parys, W.; Moeyersoon, B.; Van Thourhout, D.; Baets, R.; Vanwolleghem, M.; Dagens, B.; Decobert, J.; Le Gouezigou, O.; Make, D.; Vanheertum, R.; Lagae, L. Transverse Magnetic Mode Nonreciprocal Propagation in an Amplifying AlGaInAs/InP Optical Waveguide Isolator. *Appl. Phys. Lett.* **2006**, *88*, 2004–2007.

(12) Yu, Z.; Fan, S. Complete Optical Isolation Created by Indirect Interband Photonic Transitions. *Nat. Photonics* **2009**, *3*.

(13) Lira, H.; Yu, Z.; Fan, S.; Lipson, M. Electrically Driven Nonreciprocity Induced by Interband Photonic Transition on a Silicon Chip. *Phys. Rev. Lett.* **2012**, *109*, 1–5.

(14) Stern, B.; Zhu, X.; Chen, C. P.; Tzuang, L. D.; Cardenas, J.; Bergman, K.; Lipson, M. On-Chip Mode-Division Multiplexing Switch. *Optica* **2015**, *2*, 530.

(15) Ross, C. A.; Tepper, T.; Avrahami, Y. Magnetooptical Isolator Material. US7006289 B2, 2002.

(16) Yanaga, M.; Shoji, Y.; Takamura, Y.; Nakagawa, S.; Mizumoto, T. Compact Magnetooptical Isolator with Cobalt Ferrite on Silicon Photonic Circuits. *Appl. Phys. Express* **2015**, *8*, 082201.

(17) Yokoi, H.; Mizumoto, T.; Shinjo, N.; Futakuchi, N.; Nakano, Y. Demonstration of an Optical Isolator with a Semiconductor Guiding Layer That Was Obtained by Use of a Nonreciprocal Phase Shift. *Appl. Opt.* **2000**, *39*, 6158–6164.

(18) Shoji, Y.; Mizumoto, T.; Yokoi, H.; Hsieh, I. W.; Osgood, R. M. Magneto-Optical Isolator with Silicon Waveguides Fabricated by Direct Bonding. *Appl. Phys. Lett.* **2008**, *92*.

(19) Tien, M.-C.; Mizumoto, T.; Pintus, P.; Kromer, H.; Bowers, J. E. Silicon Ring Isolators with Bonded Nonreciprocal Magneto-Optic Garnets. *Opt. Express* **2011**, *19*, 11740–11745.

(20) Sung, S.-Y.; Sharma, A.; Block, A.; Keuhn, K.; Stadler, B. J. H. Magneto-Optical Garnet Waveguides on Semiconductor Platforms: Magnetics, Mechanics, and Photonics. *J. Appl. Phys.* **2011**, *109*, 07B738.

(21) Hutchings, D. C.; Holmes, B. M.; Zhang, C.; Dulal, P.; Block, A. D.; Sung, S.-Y.; Seaton, N. C. a.; Stadler, B. J. H. Quasi-Phase-Matched Faraday Rotation in Semiconductor Waveguides With a Magnetooptic Cladding for Monolithically Integrated Optical Isolators. *IEEE Photonics J.* **2013**, *5*, 6602512–6602512.

(22) Ghosh, S.; Keyvavinia, S.; Van Roy, W.; Mizumoto, T.; Roelkens, G.; Baets, R. Ce:YIG/Silicon-on-Insulator Waveguide Optical Isolator Realized by Adhesive Bonding. *Opt. Express* **2012**, *20*, 1839–1848.

(23) Shoji, Y.; Miura, K.; Mizumoto, T. Optical Nonreciprocal Devices Based on Magneto-Optical Phase Shift in Silicon Photonics. *J. Opt.* **2016**, *18*, 013001.

(24) Qi, W.; Jin, Y.; Yu, H.; Jiang, X. A Magneto-Optical Isolator Based on Series-Coupled Race-Track Resonators. *Jpn. J. Appl. Phys.* **2014**, *54*, 012601.

(25) Sun, X. Y.; Du, Q.; Goto, T.; Onbasli, M. C.; Kim, D. H.; Aimon, N. M.; Hu, J.; Ross, C. A. Single-Step Deposition of Cerium-Substituted Yttrium Iron Garnet for Monolithic On-Chip Optical Isolation. *ACS Photonics* **2015**, *2*, 856–863.

(26) Goto, T.; Onbasli, M. C.; Kim, D. H.; Singh, V.; Inoue, M.; Kimerling, L. C.; Ross, C. a. A Nonreciprocal Racetrack Resonator Based on Vacuum-Annealed Magnetooptical Cerium-Substituted Yttrium Iron Garnet. *Opt. Express* **2014**, *22*, 19047.

(27) Tien, M.-C.; Mizumoto, T.; Pintus, P.; Kromer, H.; Bowers, J. E. Silicon Ring Isolators with Bonded Nonreciprocal Magneto-Optic Garnets. *Opt. Express* **2011**, *19*, 11740–11745.

(28) Bi, L.; Hu, J.; Jiang, P.; Kim, D. H.; Dionne, G. F.; Kimerling, L. C.; Ross, C. A. On-Chip Optical Isolation in Monolithically Integrated Non-Reciprocal Optical Resonators. *Nat. Photonics* **2011**, *5*, 758–762.

(29) Pintus, P.; Di Pasquale, F.; Bowers, J. E. Integrated TE and TM Optical Circulators on Ultra-Low-Loss Silicon Nitride Platform. *Opt. Express* **2013**, *21*, 5041–5052.

(30) Bi, L.; Hu, J.; Dionne, G. F.; Kimerling, L.; Ross, C. A. Monilithlic Integration of Chalcogenide Glass/iron Garnet Waveguides and Resonators for on-Chip Non Reciprocal Photonic Devices. *Int. Soc. Opt. Photonics.* **2011**, *7941*, 794105–794105 – 10.

(31) Shintaku, T.; Uno, T. Optical Waveguide Isolator Based on Nonreciprocal Radiation Optical Waveguide

Isolator Based on Nonreciprocal Radiation. *J. Appl. Phys.* **1994**, *76*.

(32) Pintus, P.; Di Pasquale, F.; Bowers, J. E. Design of Transverse Electric Ring Isolators for Ultra-Low-Loss Si3N4 Waveguides Based on the Finite Element Method. *Opt. Lett.* **2011**, *36*, 4599–4601.

(33) Holmes, B. M.; Hutchings, D. C. Demonstration of Quasi-Phase-Matched Nonreciprocal Polarization Rotation in III-V Semiconductor Waveguides Incorporating Magneto-Optic Upper Claddings. *Appl. Phys. Lett.* **2006**, *88*, 3–5.

(34) Vogel, M.; Chumak, A. V; Waller, E. H.; Langner, T.; Vasyuchka, V. I.; Hillebrands, B.; Freymann, G. Von. Optically Reconfigurable Magnetic Materials. *Nat. Phys.* **2015**, *11*.

(35) Sun, D.; Schooten, K. J. Van; Kavand, M.; Malissa, H.; Zhang, C.; Groesbeck, M.; Boehme, C.; Vardeny, Z. V. Spin – Orbit Coupling. *Nat. Mater.* **2015**, *15*, 863–870.

(36) Jaworski, C. M.; Yang, J.; Mack, S.; Awschalom, D. D.; Heremans, J. P.; Myers, R. C. Observation of the Spin-Seebeck Effect in a Ferromagnetic Semiconductor. *Nat. Mater.* **2010**, *9*, 898–903.

(37) Kirihara, A.; Uchida, K.; Kajiwara, Y.; Ishida, M.; Nakamura, Y.; Manako, T.; Saitoh, E.; Yorozu, S. Spin-Current-Driven Thermoelectric Coating. *Nat. Mater.* **2012**, *11*, 686–689.

(38) An, T.; Vasyuchka, V. I.; Uchida, K.; Chumak, A. V; Yamaguchi, K.; Harii, K.; Ohe, J.; Jungfleisch, M. B.; Kajiwara, Y.; Adachi, H.; Hillebrands, B.; Maekawa, S.; Saitoh, E. Unidirectional Spin-Wave Heat Conveyer. *Nat. Mater.* **2013**, *12*, 549–553.

(39) Burrowes, C.; Heinrich, B.; Kardasz, B.; Montoya, E. A.; Girt, E.; Sun, Y.; Song, Y.; Wu, M. Enhanced Spin Pumping at Yttrium Iron Garnet / Au Interfaces Enhanced Spin Pumping at Yttrium Iron Garnet / Au Interfaces. *Appl. Phys. Express* **2016**, *092403*, 3–7.

(40) Heinrich, B.; Burrowes, C.; Montoya, E.; Kardasz, B.; Girt, E.; Song, Y.; Sun, Y.; Wu, M. Spin Pumping at the Magnetic Insulator (YIG)/ Normal Metal (Au) Interfaces. *Phys. Rev. Lett.* **2011**, *066604*, 1–4.

(41) Kurebayashi, H.; Dzyapko, O.; Demidov, V. E.; Fang, D.; Ferguson, A. J.; Demokritov, S. O. Controlled Enhancement of Spin-Current Emission by Three-Magnon Splitting. *Nat. Mater.* **2011**, *10*, 660–664.

(42) Serga, A. A.; Chumak, A. V; Hillebrands, B. YIG Magnonics. *J. Phys. D; Appl. Phys.* **2010**, *264002*.

(43) Uchida, K.; Xiao, J.; Adachi, H.; Ohe, J.; Takahashi, S.; Ieda, J.; Ota, T.; Kajiwara, Y.; Umezawa, H.; Kawai, H.; Bauer, G. E. W.; Maekawa, S.; Saitoh, E. Spin Seebeck Insulator. *Nat. Mater.* **2010**, *9*, 894–897.

(44) Gruszecki, P.; Kasprzak, M.; Serebryannikov, A. E.; Krawczyk, M.; Śmigaj, W. Microwave Excitation of Spin Wave Beams in Thin Ferromagnetic Films. *Sci. Rep.* **2016**, 1–8.

(45) Hutchings, D. C.; Holmes, B. M. A Waveguide Polarization Toolset Design Based on Mode Beating. *IEEE Photonics J.* **2011**, *3*, 450–461.

(46) Sekijima, T.; Kishimoto, H. Magnetic, Optical and Microwave Properties of Rare-Earth-Substituted Fibrous Yttrium Iron Garnet Single Crystals Grown by Floating Zone Method. *Jpn. J. Appl. Phys.* **1999**, *38*, 5874.

(47) Shintaku, T.; Tate, A.; Mino, S. Ce-Substituted Yttrium Iron Garnet Films Prepared on GdScGaO Garnet Substrates by Sputter Epitaxy. *Appl. Phys. Lett.* **1997**, *71*, 1640.

(48) Block, A. D.; Dulal, P.; Stadler, B. J. H.; Seaton, N. C. A. Growth Parameters of Fully Crystallized YIG, Bi:YIG, and Ce:YIG Films With High Faraday Rotations. *IEEE Photonics J.* **2014**, *6*, 1–8.

(49) Wolfe, R.; Fratello, V. J.; McGlashan Powell, M. Thin-Film Garnet Materials with Zero Linear Birefringence for Magneto-optic Waveguide Devices. *J. Appl. Phys.* **1988**, *63.8*, 3099–3103.

(50) Licht, S. J. Technique for Controlled Adjustment of Bubble Collapse Field in Epitaxial Garnet Films by Etching. *J. Electron. Mater.* **1975**, *4.4*, 757–768.